Journal of the Meteorological Society of Japan, Vol. 82, No. 5, pp. 1301–1314, 2004

Application of Double-Fourier-series Spectral Method to a Large Size Problem: Two-dimensional Simulations of the Shear Instability on the Sphere

In-Hyuk KWON, Hyeong-Bin CHEONG

Dept. of Environmental Atmospheric Sciences, Pukyong National University, Pusan, Korea

Minsu JOH

Supercomputing Center, Korea Institute of Science and Technology Information, Daejeon, Korea

Il-Ung CHUNG

Dept. of Atmospheric and Environmental Sciences, Kangnung National University, Kangnung, Korea

Chun-Ho CHO

Forecast Research Lab., Meteorological Research Institute, Korea Meteorological Administration (KMA), Seoul, Korea

and

Woo-Jin LEE

Numerical Weather Prediction division, Korea Meteorological Administration (KMA), Seoul, Korea

(Manuscript received 16 June 2003, in final form 13 May 2004)

Abstract

Double-Fourier-Series (DFS) spectral method is applied to a large-size problem of barotropic instability of double-shear flow on the sphere. The computing source is the NEC SX-5 parallel vector processors, with the maximum vector length of 512. It is demonstrated that the DFS spectral model is robust and stable even for such a large-sized intensively nonlinear problem, and can simulate well the multiple scale phenomenon without losing accuracy. In addition to the efficiency on serial computing, represented with $O(N^2 \log_2 N)$ operations as opposed to $O(N^3)$ for the spherical harmonics spectral method, with N the truncation, the DFS spectral model also preserves the efficiency on parallel computing on vector architecture, due to its nature of two dimensional transform. The parallel performance increased slightly with the resolution, and nearly 33.5 percent (26.8 GFLOPS) of the theoretical peak performance (80 GFLOPS) was achieved in the highest-resolution experiment.

Corresponding author: Hyeong-Bin Cheong, Dept. of Environmental Atmospheric Sciences, Pukyong National University, 599-1 Daeyeon 3-cong, Nam-gu, Pusan 608-737, Korea.
E-mail: hbcheong@pknu.ac.kr

The zonal-mean absolute vorticity, of which initial condition is characterized as two peaks in both hemispheres, evolves with time into a nearly constant value over the hemisphere. On the other hand, the meridional gradient of the absolute vorticity increases around the equator. The kinetic energy per unit mass is calculated for each total wavenumber, where a disturbance field of a single total wavenumber is separated by an 8th-order spherical harmonics filter. Kinetic energy spectrum shows two distinct subranges, each with a constant slope. The subrange, other than the viscous subrange, shows a slightly increasing slope with time and approaches l^{-3} (l is the total wavenumber) in the matured stage, when a single large vortex is formed. As the resolution increases, the subrange other than the viscous subrange extends to the higher wavenumber domain, due to low viscosity. Numerical convergence of the solution with a fixed viscosity is discussed in terms of time averaged zonal-mean statistics of the zonal-flow.

1. Introduction

The computation of atmospheric flows over the spherical domain requires an elaborate numerical method to avoid the so-called pole problem, which is a collective term referring to the numerical problems near poles arising from the use of spherical coordinates. In the traditional Finite Difference Method (FDM) the pole problem is circumvented by introducing the Fourier filtering for moderate resolutions, but it is not certain that it would still be effective at high resolutions. At higher resolutions, the global treatment, rather than a local treatment, of the problem may be more essential (e.g., Spotz et al. 1998; Cheong 2000a,b; Cheong et al. 2002) in the context of the spurious global mode inherent in a spherical-domain dynamic frame.

The spectral method adopting the spherical harmonics as the orthogonal basis functions, most widely used for the global numerical weather prediction models (Gates et al. 1992; see also *http://www-pcmdi.llnl.gov/amip/* which is lastly updated in Feb 2001), is free from the pole problem, because the spherical harmonics provide the even resolution over the sphere, and the spatial differentiation is performed in the spectral domain. The Spherical Harmonics Model (SHM), however, has major drawbacks at high resolution, such as the huge computational cost and the communication overhead on distributed memory architectures. A more serious problem than these inefficiencies is that the accuracy of orthogonality of the discrete Legendre functions decreases at resolutions much higher than the current models (e.g., Jakob et al. 1995).

The computational difficulties stated above certainly put restrictions on the maximum problem size (resolution) even for the two dimensional models. Recently, several numerical methods have been developed to overcome the minor points of the two major numerical methods, the FDM and SHM (Ronchi et al. 1996; Stuhne and Peltier 1996; Taylor et al. 1997; Spotz et al. 1998; Cheong 2000a). They were found to give reasonable results to simple or extended problems. Among them, Stuhne and Peltier (1996) have vividly demonstrated the performance of the newly developed method through the experiments on the strong nonlinear phenomena with an emphasis on the robustness and resolvability of the complicated dynamic process. The maximum resolution therein is 163,842 geodesic grids, which roughly corresponds to the uniform latitude-longitude mesh of 60 km $\times$ 60 km. (Actually, the number of uniform latitude-longitude meshes must be $\pi/2$ times larger than that of geodesic grid cells to provide similar horizontal resolutions, due to the convergence of the grid interval off the equator.)

In this study, the two-dimensional numerical experiment is extended on the shear instability (Cheong et al. 2002), which is similar to that in Stuhne and Peltier (1996), but with double shear zones, to a large problem-size on the spherical domain. The problem size of concern exceeds 10^8 in the number of transform grid points, giving approximately 3.75 km $\times$ 3.75 km resolution (the grid size is smaller than this by 1.5 times). Though being simple, the solution of the vorticity equation has important implications in the computational fluid dynamics, because it includes nonlinear terms and needs the inversion of (high-order) a Laplacian operator.

As a computing source the high-performance computer system NEC SX-5 was used, which consists of parallel vector processors with maximum vector length of 512. Aside from the effi-

ciency in serial computing, represented with $O(N^2 \log_2 N)$ operations per a timestep, as opposed to $O(N^3)$ operations for the spherical-harmonics methodology with N the model truncation (Cheong 2000a,b), another important issue of interest in this paper is the parallel performance of the DFS spectral method on the vector architecture (cf., Cortese and Balachandar 1995).

The barotropic instability of double shear flow in this study is an extension of the barotropic instability of equatorial westerlies in Stuhne and Peltier (1996). As demonstrated in Cheong et al. (2002), to define a global normal mode is not very useful for the double shear flow on the sphere because the most unstable mode for each shear zone has a different zonal wavenumber. The flow associated with the instability of strong shears is strongly nonlinear and turbulent (Stuhne and Peltier 1996; Cheong et al. 2002). It will be of interest to see the kinetic spectrum of such a turbulent flow in a large-size problem. Yoden and Yamada (1993) studied the 2-dimensional decaying turbulence on the sphere, where the viscosity is given as a biharmonic operator and the kinetic energy spectrum was given a priori as a function of the total wavenumber. In their simulation, the spectral peak shifts toward low wavenumber as the time elapses. In the present study, a strong zonal shear is given initially, therefore it is not certain whether such a shift of peak-wavenumber and/or the same slope for the kinetic energy will be observed or not.

2. The vorticity equation and the double Fourier series spectral method

Details of the numerical simulation on the barotropic instability are the same as Cheong et al. (2002) with an exception that the hyperviscosity is used in this study. With scaling the variables by the rotation rate and radius of the Earth, the vorticity equation on the sphere is written as

$$\frac{\partial \zeta}{\partial t} = \frac{-1}{\sin^2 \phi}\left[\frac{\partial}{\partial \lambda} U\eta + \sin\phi \frac{\partial}{\partial \phi} V\eta\right] + \nu \nabla^6 \zeta, \quad (1)$$

where λ is the longitude, $\phi = \pi/2 +$ latitude, and $\eta = f + \zeta$ with $f(\equiv -2\cos\phi)$ and ζ being the Coriolis parameter and the relative vorticity, respectively. $U \equiv u \sin\phi$ and $V \equiv v \sin\phi$ with u and v being the longitudinal and latitudinal component of the velocities, respectively, and ν is the coefficient of hyperviscosity. Introducing the centered time differencing, the vorticity equation can be time marched with an implicit time-stepping with respect to the viscosity term as

$$[1 - \gamma \nabla^6]\zeta^{(p+1)} = \zeta^{(p-1)} + 2\Delta t R^{(p)}, \quad (2)$$

where R is the advection term, Δt is the time-step size and $\gamma = 2\nu\Delta t$. The superscripts denote the timesteps.

The dependent variables are expanded with the truncated double Fourier series (Cheong 2000a,b), e.g.,

$$g_m(\phi) = \begin{cases} \sum_{n=0}^{N} g_{m,n} \cos n\phi \\ \quad \text{for } m = 0, \\ \sum_{n=1}^{N} g_{m,n} \sin n\phi \\ \quad \text{for odd } m, \\ \sum_{n=1}^{N} g_{m,n} \sin\phi \sin n\phi \\ \quad \text{for even } m(\neq 0), \end{cases} \quad (3)$$

where $g_m(\phi)$ represents the zonal Fourier transform of $g(\lambda, \phi)$. N is the maximum meridional-wavenumber or the truncation, which is set the same as the zonal-wavenumber truncation M.

Transform method is used for the evaluation of the nonlinear terms (Orszag 1970; Cheong 2000a), and the number of transform grid points, with uniform latitude-longitude, is given as $(I \times J) = (2^k \times 2^{k-1})$, where if not otherwisely stated we take $k = 12, 13$, and 14. The maximum wavenumbers adequate for each grid resolution are determined by the 2/3 rule (see Table 1 for model parameters). To determine an appropriate value of the viscosity coefficient ν is rather difficult (see also Stuhne and Peltier 1996), because the flow field is sensitive to the viscosity and the flow field in turn affects the numerical stability for a given time-step size. Through experiments with wide range of parameters we found that the minimum viscosity should be given $\nu = (100/2\pi)[3.75^{\log_2(M/170)-1}][M(M+1)]^{-3}$ for stable time-integration in this problem. The viscosity coefficient ν in Table 1 is larger than this value

Table 1. Wavenumber truncations and the number of transform grid points. The viscosity is presented in nondimensional unit.

model	transform grids ($I \times J$)	time-step (Δt)	viscosity (ν)	total memory
M1364	4096×2048	32 sec	0.190×10^{-15}	2.0 GB
M2728	8192×4096	16 sec	0.113×10^{-16}	9.7 GB
M5460	16384×8192	8 sec	0.600×10^{-18}	32.1 GB

for each resolution. Although the timestep size used in this study is slightly in excess of that estimated by the CFL criteria for the spectral model, the time integration could be done without numerical instability because the small scale disturbances near the truncation limit are severely dampened down by the hyperviscosity.

Note that the memory requirement for M5460 resolution is as large as 32 GB even though two dimensional problem is solved, but this is not surprising if it is considered that the array size for a field variable exceeds one GB. In the case of the spherical harmonics model, the memory space for $M \times N \times (J/2)$ elements is necessary to store the associated Legendre functions and their derivatives, which corresponds to nearly 1,000 GB for double precision arrays.

Although being possible, the reduced grids near the poles (Hortal and Simmons 1991) are not used in this study, because it could invite the computational inefficiency in the aspect of the vectorization of the codes. Instead, the polar Fourier filtering in the zonal-Fourier space is carried out to achieve the almost even resolution over the sphere:

$$g_m(\phi) \to 0 \quad \text{for } |m| > \frac{M \sin\phi}{\sin(\pi/6)}. \tag{4}$$

The equivalent mesh sizes are approximately 15 km $\times$ 15 km, 7.5 km $\times$ 7.5 km and 3.75 km $\times$ 3.75 km for M1364, M2728 and M5460, respectively, while the grid sizes, calculated by dividing $2\pi\times$ Earth's radius by zonal grid number, are smaller than these by about 1.5 times.

The initial conditions for the zonal mean flow, and the absolute vorticity, are the same as Fig. 3 in Cheong et al. (2002). The model is run for 100 model-days for all resolutions except that M5460 case is run for 50 model days, due to the limitation of computing power. One timestep needs floating-point operations as many as 48×10^9 for M5460 resolution. Therefore such a heavy computational task can only be accomplished by the high-performance computers.

Table 2. Details of the computing source used in this study

model	NEC SX-5
number of CPU	8
theoretical peak performance	80 GFLOPS
system memory	128 GB
vector resister length	512

3. Optimization of the codes

Details on the computing source used in this study are presented in Table 2. Since NEC SX-5 consists of Parallel Vector Processors (PVP), the optimization of the codes can be done in two contexts: the vectorization and parallel implementation. Parallel implementation was carried out in two ways: One is the Open Specifications for Multi-Processing (OpenMP, Chandra et al. 2000; see also the web page www.openmp.org[1]), and the other is the micro-task directives. Both are suitable for a shared-memory architecture such as NEC SX-5[2]. It was revealed that the parallel performance for both cases was almost the same for the problem treated in this study. Obviously, the vectorization is of a primary importance because the number of the vector resistors within a CPU is larger than the number of CPU by nearly two order. The parallelism is given in the next section. To enhance the computational efficiency as much as possible, the elaborate programming techniques (e.g., Sabot 1995; Ilin and Scott 1996) were fully taken into consideration.

The overview of the vorticity-equation solver for one time-stepping is illustrated in Table

1 This web page is managed by the OpenMP Architecture Review Board.

2 Details on the multi-tasking are found at FORTRAN90/SX Multitasking User's Guide, NEC Corporation; http://www.atmosp.physics.utoronto.ca/SX5/docs/g1af08e/frame.html.

3. The operation count for all steps is $O(N^2)$ except for the FFT routine, which needs $O(N^2 \log_2 N)$ operations. It is found that most of the computing time is used for six modules. Consequently the optimization of these modules will be a key factor to get an optimized use of the NEC SX-5. By the functions, the seven modules are classified into three categories, the double FFT, inversion and nonlinear terms evaluation. The major two categories are explained below in some detail.

3.1 *Double FFT (Fast Fourier Transform) over the sphere*

The transform from the grid to spectral space, $X(i,j) \rightarrow X(m,n)$, is carried out using double FFT, which consists of five steps as shown below. The inverse transform is done in the reversed order. Both transforms are performed in the module SUB_2, which is called totally five times per one timestep from the main program, and the subroutine SUB_6 (used for evaluation of advection terms), as shown in Table 3.

(i) Transpose the array of grid data $(X_{i,j} \rightarrow X_{j,i})$

(ii) Fourier transform in longitude $(X_{j,i} \rightarrow X_{j,m})$ by calling SUB_3: SUB_3 is a routine for the Fourier (inverse) transform of two dimensional real data with the length being a power of 2. It calls SUB_1, a routine for the complex Fourier transform. In this step J transforms are necessary. All routines are readily vectorized by taking 'the *do loop* for the first array axes' as the innermost loop nest (Sabot 1995). Although the vectorization process requires a two-dimension data movement, instead of one-dimension data for a sequential processing, it does not cause a serious problem.

(iii) Polar Fourier filtering of $(X_{j,m})$ as in Eq. (4)

(iv) Transpose the array of zonal Fourier transform $(X_{j,m} \rightarrow X_{m,j})$ and combine the odd and neighboring even zonal-wavenumber Fourier components to make a 2π-length data (that is, M sets of $2J$ data points).

(v) Fourier transform in latitude $(X_{m,j} \rightarrow X_{m,n})$ by calling SUB_3 again: Only M transforms are necessary in this step.

3.2 *Inversion of tri- or pentadiagonal matrices*

The step (ii) in Table 3 is the inversion of tridiagonal matrices, while the step (xii) inverts the pentadiagonal matrices. The matrices are time-invariant during the time integration, thus a prehandling of them will help reduce the operation count. An example for the tridiagonal matrices is given in the Appendix. The routine for the pentadiagonal matrices inversion is similar to the tridiagonal case, but the operation count is nearly doubled. An updated pentadiagonal matrices solver can be found in Cheong et al. (2004).

Table 3. Overview of the vorticity-equation solver for one time-stepping. The subscripts (i,j) represent the grid indices and (m,n) the wave indices.

step	procedure	method
(i)	$\zeta^{(p)}_{m,n} \rightarrow \zeta_{i,j}$	(FFT)
(ii)	$\zeta^{(p)}_{m,n} \rightarrow \psi_{m,n}$	(inversion)
(iii)	$\psi_{m,n} \rightarrow U_{m,n}$	
(iv)	$\psi_{m,n} \rightarrow V_{m,n}$	
(v)	$U_{m,n} \rightarrow U_{i,j}$	(FFT)
(vi)	$V_{m,n} \rightarrow V_{i,j}$	(FFT)
(vii)	$U_{i,j} \cdot \zeta_{i,j} \rightarrow X_{i,j}$	
(viii)	$V_{i,j} \cdot \zeta_{i,j} \rightarrow Y_{i,j}$	
(ix)	$X_{i,j} \rightarrow X_{m,n}$	(FFT)
(x)	$Y_{i,j} \rightarrow Y_{m,n}$	(FFT)
(xi)	$\left\{ \begin{matrix} \zeta^{(p-1)}_{m,n} \\ X_{m,n} \\ Y_{m,n} \end{matrix} \right\} \rightarrow Z_{m,n}$	
(xii)	$Z_{m,n} \rightarrow \zeta^{(p+1)}_{m,n}$	(inversion)

Table 4. CPU time for one timestep and execution rate on a single CPU of NEC SX-5. The numerals in the parenthesis are the relative execution time to that for M1364.

resolution	Execution time (second)	Execution rate (MFLOP)
M1364	0.549 (1.00)	4,790
M2728	2.285 (4.16)	4,874
M5460	9.632 (17.54)	4,975

4. Computing time and parallel performance

In Table 4, the overall performance of the NEC SX-5 on the vorticity-equation solver

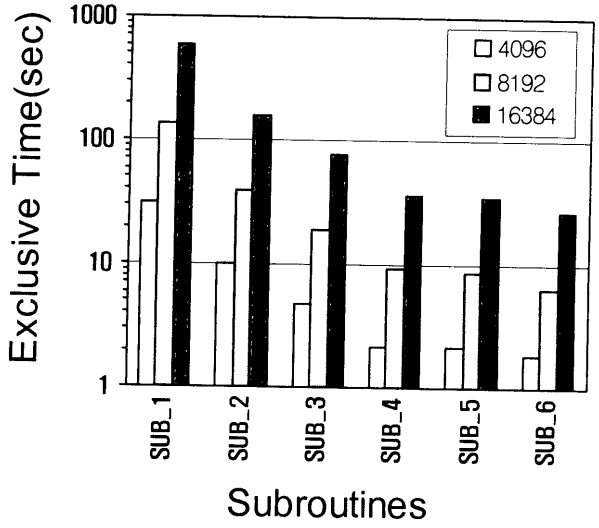

Fig. 1. Real execution time for 273 timesteps required for the major six subprograms included in the vorticity-equation solver with DFS. The numerals in the box denote the number of longitudinal grid points. The functions of the subroutines above are, from left to right, the complex FFT, transform of variables for complex- or real-FFT, real FFT, high-order spectral filtering, inversion of Laplacian operator, and evaluation of advection terms, respectively.

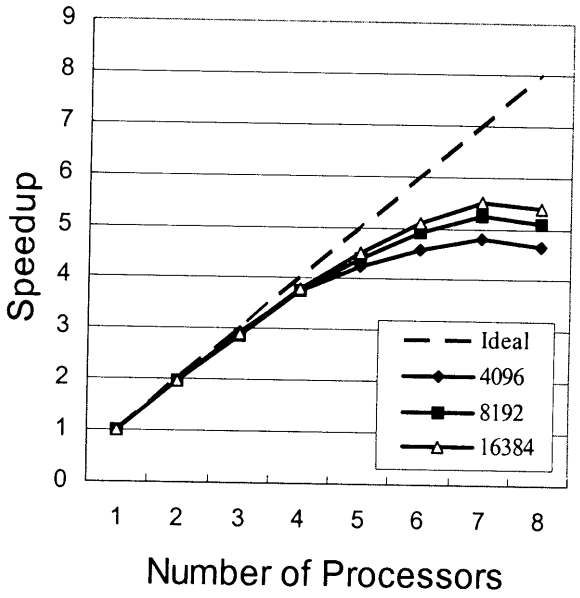

Fig. 2. Variation of speedup with the number of CPUs used for three resolutions. The numerals denote number of the zonal gridpoints.

is presented in terms of the CPU time and floating-point execution rate. First it is noted that the execution time for one timestep increases with the resolution, closely following the theoretically expected operation count $O(N^2 \log_2 N)$. The execution rate increases slightly with the resolution, which demonstrates a desirable scalability of the programs[3]. The mean execution rate for these resolutions is nearly half of the theoretical peak performance of a CPU. In average the Vectorized Operation Ratio (VOpR), being a measure of the efficiency available through vectorization, reaches about 99.7% for all resolutions.

Real execution times for the major six modules are shown in Fig. 1 for three model resolutions. The ratios of the major three modules, SUB_1, SUB_2 and SUB_3 (see the figure caption for the function of these subroutines), to the total CPU time are 70%, 15% and 8%, respectively, which do not vary substantially with the resolution, indicating that all modules are well vectorized and scalable.

For the vector architectures, the parallelism can be implemented in two ways in the case of a multi-dimension problem, depending on what level do-loop is split. One is to split the innermost (lowest) do-loop, and the other is to split the higher level of loop nest. It appears that the second choice will be better, because the first method can harm the vector execution by shortening the length of the lowest level do-loop. In spite of this fact, we adopted the first method for a certain routine such as FFT, which inherently renders difficulty in parallelism (see Press et al. 1996). Fortunately, even in that case, such a disadvantage is rather low because the vector length of the innermost do-loop is quite long.

In Fig. 2 the variation of CPU time with the number of CPU is presented. Speedup factor is very close to the ideal parallel performance for two CPUs, but the performance gap between the ideal performances becomes large

3 Definition of the scalability of a program or a scalable program includes also the portability of a program across different architectures (Sabot 1995).

as the number of CPU increases. Nevertheless, a maximum speedup by a factor of 5.55 is achieved for 7 CPUs at M5470 resolution, which is considered as a desirable parallel performance[4]. This again shows a fairly good resolution-scalability of the programs. It is worthy noting that the parallel-speedup slowly decreases as the resolution decreases, being considered as a direct consequence of the first method chosen for FFT routine stated above.

5. Results of the simulation

In this section, some simulation results are presented. The advantage of using a very-high-resolution model would be the reproducibility of the multiscale phenomena interacting one another within a single dynamics. Therefore, it must be of a central importance to compare how the small scales are well resolved in the high-resolution models. A typical time evolution of the vorticity field, with the resolution M340, is illustrated in Fig. 4 of Cheong et al. (2002): In the first few days the unstable waves develop as a result of shear instability with dominant wavenumber of 7 or 8 in low latitude shear-zone, which finally grow into isolated vortices. During model days from 6 to 10 an intense interaction among vortices and the generation of small-scale vortices are observed. In all experiments, the final stage of the flow evolution is characterized by the formation of a large single vortex, although the location and the structure are different from experiment to experiment (see also Stuhne and Peltier 1996) due to the strong nonlinear nature of the flows.

The left column of Fig. 3 presents the absolute vorticity field at day 6 for three resolutions, with the northern-hemisphere stereographic projection, where large-scale features are dominant. Since the overall synoptic pattern is of concern, the contour values are omitted in this map. Although they look similar to one another, detailed distribution of the absolute vorticity differs substantially, which is an indication of chaotic behavior of the dynamic system, because the initial conditions are actually the same. Shown in the right column of Fig. 3 are the absolute vorticity over a small domain, which is between 14 N and 37 N in latitude and extends over 26 degrees in longitude, respectively. It is clear that the vortex elongates more as the model resolution increases. That is, thinner vortex-filaments are observed at increased resolutions, as it was expected to be. On the other hand, thin vortex filaments for low resolutions are easily dissipated due to relatively large viscosity.

The high-resolution simulations well produce the isolated vortices of small-scale, which is reflected in the kinetic energy spectrum presented below. In some cases of high-resolution simulations, second barotropic instability occurs in the course of rolling up of the thinning vortex filaments, of which related scale is one or two order small compared to the unstable waves developing by the initial zonal shear (see Fig. 4). This instability is due to the large vorticity gradient as manifested by the multiple spiral bands of red-colored filament over the northern edge of the large vortex.

Incorporation of the viscosity in the model is generally two fold: One is to mimic simply the physical dissipation mechanism, and the other is to maintain the numerical stability. For the second purpose, the viscosity must be as small as possible. However, too small numerical-viscosity does not contribute to the stability of the model at high resolutions, while the viscosity either physical or numerical invites unwanted damping of the conserved quantity. Therefore, the loss of a conserved quantity during time integration is another reasonable measure of the model performance.

Table 5 presents the total kinetic-energy (TKE) loss for selected days, normalized by the initial TKE. By day 50 the model M2728 conserves the kinetic energy with the loss of only about 0.01% of the initial value, although the viscosity was not taken as the minimum level allowed for each resolution. This suggests that the TKE can be better conserved by diminishing the viscosity. It is worth noting that the TKE loss becomes smaller with the resolution,

4 The parallel performance decreases at 8CPUs case. This corresponds to the case using total CPUs available. We additionally carried out the same computations on the NEC SX-5 system in the Korea Meteorological Administration. Even in that case, if all CPUs (i.e., 16 CPUs) are used for parallel computing, such a decrease in speedup is observed at the 16 CPUs case. This is because one CPU is allocated to the administration of the parallel computing when all CPUs available are used.

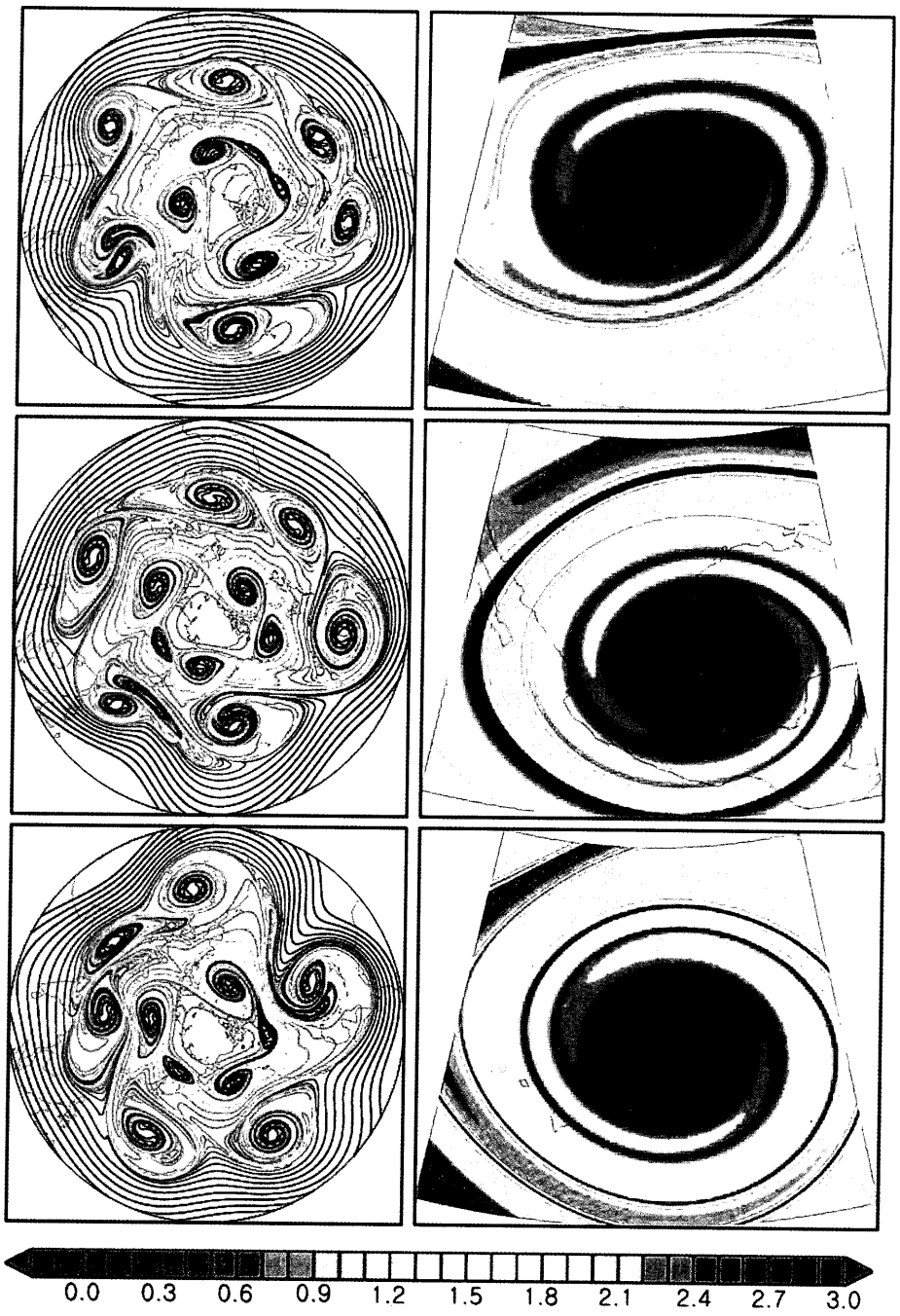

Fig. 3. Absolute vorticity field at day 6, scaled by the rotation rate of the Earth. Left column: global pattern with the northern-hemisphere stereographic projection. Right column: zoomed view of a small area, whose map domains are between 14 N and 37 N in latitude and extend over 26 degrees in longitude, respectively. From above, the resolutions are M1364, M2728 and M5460, respectively.

which implies that the conservation property is not saturated even for such a huge problem size. Of course, we believe that this result can not be extended to general cases. Not shown, beyond day 50 the TKE does not vary significantly, because the intense nonlinear interaction in the flow field was almost finished before day 50.

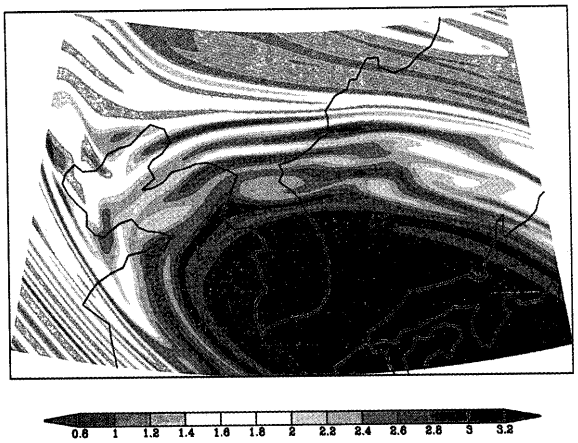

Fig. 4. Absolute vorticity field at 11.2 day for M5460, scaled by the rotation rate of the Earth. Map domain is (33.03 N, 116.5 E)–(44.03 N, 139.0 E).

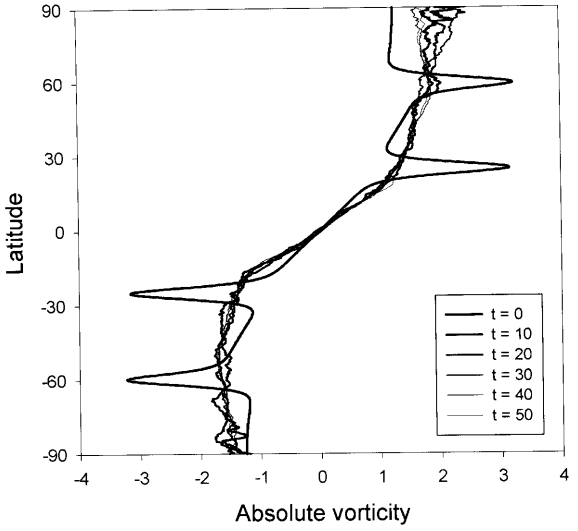

Fig. 5. Zonal-mean absolute vorticity at selected days for M2728, scaled by the rotation rate of the Earth.

Some important aspects of the simulations, either in numerical or dynamical view point, are described below.

5.1 Vorticity mixing

The model used in this study is the vorticity equation in which the global mean absolute vorticity is conserved with time in the absence of viscosity. On the other hand, the unstable waves developing at the shear zone modify the zonal-mean flow through zonal momentum exchanges. As a result the shear of the initial zonal-mean flow becomes weak. Figure 5 presents the zonal-mean absolute vorticity at selected days for various resolutions. By day 5, the peaks of zonal-mean absolute vorticity almost disappears. Beyond day 10, a nearly constant value is observed within a hemisphere with small-scale fluctuations. That is, the absolute vorticity is well distributed over the hemisphere by the turbulent motions accompanying the breaking of barotropic unstable waves. By day 50, the small-scale fluctuations almost disappeared, leaving a very smooth variation of absolute vorticity with latitude. The time variation of the absolute vorticity around the equator is somewhat different: Its meridional gradient becomes larger than the initial stage, probably due to the vorticity homogenization in positive (negative) value in the northern (southern) hemisphere.

5.2 Numerical convergence of the solution

As we have seen above, the high resolution run with small diffusion captures the fine structure of the flow field which can not be observed in low resolution simulations. Any difference of physical parameters in the vorticity equation brings about the difference in the solution. From the viewpoint of solution of partial differential equation, it would be important to see how the numerical solution converges with a fixed diffusion coefficient. Since the flow field

Table 5. Normalized total kinetic energy loss with time

resolution	time (day)						
	1	2	5	10	20	30	50
M1364	0.75E−7	0.11E−5	0.41E−4	0.11E−3	0.18E−3	0.20E−3	0.24E−3
M2728	0.24E−6	0.87E−6	0.19E−4	0.46E−4	0.87E−4	0.10E−3	0.12E−3
M5460	0.22E−5	0.34E−5	0.63E−5	0.99E−5	0.14E−4	0.21E−4	0.33E−4

is chaotic, we do not expect that the flow fields for different resolutions are the same at a fixed temporal position. The convergence of solution is often checked by comparing the zonal-time mean statistics for such a chaotic system (e.g., Held and Suarez 1994).

For this comparison, the nondimensional viscosity ν is given as 6.479×10^{-13} for all resolutions, and the data are sampled with 0.1 day interval. Figure 6 presents the zonal-mean zonal flows, averaged in the period from day 70 to day 100, for three low resolutions of $I = 512, 1024$ and 2048, along with the initial zonal-mean profile. The initial zonal-mean flow is modified to a large extent almost in the global domain, as stated above. The equatorial westerly, however, is almost unchanged in spite of the presence of strong vortices which move in a wide range of latitudes. Note that the zonal flow for $I = 1024$ is different from that of $I = 512$: The maximum difference reaches about 10 *m/s* at middle latitudes. However, the difference decreases to a fairly lower level in all latitudes for the cases $I = 1024$ and 2048. The largest value falls within a couple of *m/s*. As described above, in the final stage a large, single migrating-vortex is formed. In relation with this vortex, the zonal-mean flow has time-fluctuation, with a period of nearly 10-days. Considering that the amplitude of fluctuation exceeds 15 *m/s* (not shown), the difference between $I = 1024$ and 2048 is not regarded to be significant.

5.3 *Energy spectrum of the flow field*

In the simulations, the total kinetic energy dissipates monotonically with time because no energy source exists and the hyperviscosity is included. The energy spectrum for the decaying turbulent is of interest in the geophysical-fluid point of view. In order to see the kinetic energy spectrum with the horizontal scale, we must decompose the flow field into each horizontal scales. On the spherical surface a two-dimensional scale is well defined in terms of the total wavenumber l as in the spherical harmonics $P_l^m(\sin\theta)\exp(im\lambda)$, where θ is the latitude. Decomposition of the global data into the spherical-harmonics components can be done via the Gauss-Legendre transform. This

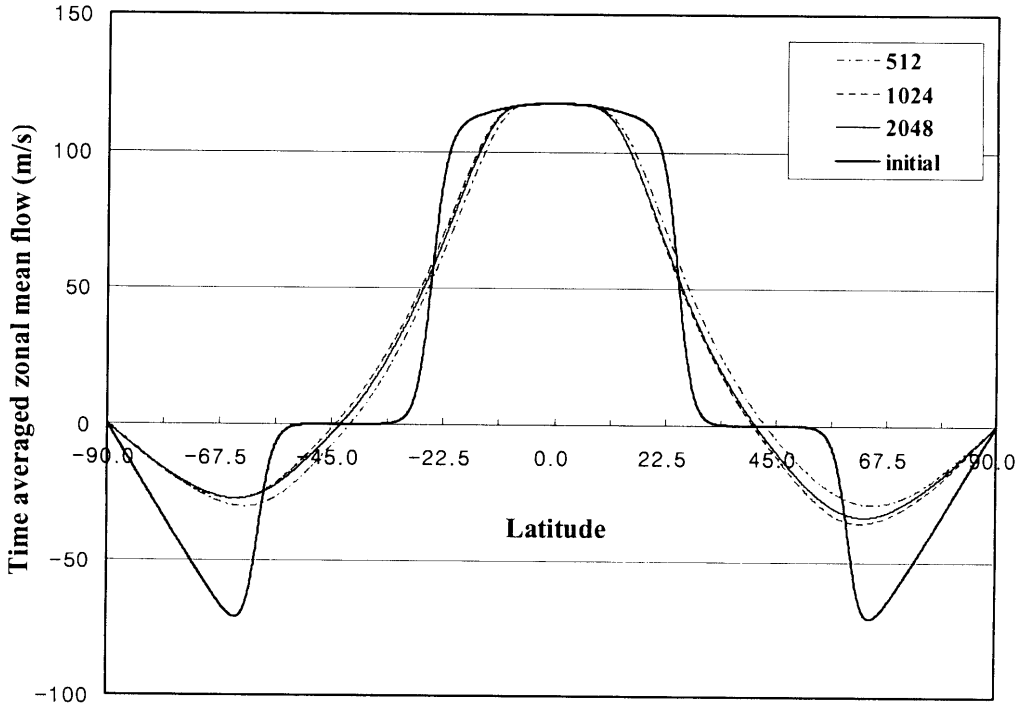

Fig. 6. Zonal-mean of the zonal flow, averaged for 30 days from day 70 to day 100. The viscosity is given the same value for all cases shown in this figure.

requires a huge computation as well as the calculation and storage of the spherical harmonics, particularly for the high-resolution data. In this study, as an alternative, we incorporate the 8th order spherical-harmonics spectral filter with DFS, which can provide a sharp cutoff of the wave components smaller than a prescribed scale (Cheong et al. 2004).

To separate a certain horizontal-scale, say l, from the vorticity field ζ, two times of high-order spherical-harmonics filtering are required:

$$(1 + a_l \nabla^{16})\zeta_l = \zeta,$$
$$(1 + a_l^* \nabla^{16})\zeta_l^* = \zeta, \tag{5}$$

where $a_l = 2/[l(l+1)]^8$, $a_l^* = 2/[(l+1)(l+2)]^8$, and ζ_l and ζ_l^* represent the filtered variables. Then, the difference between two filtered fields $\zeta_l^f (\equiv \zeta_l^* - \zeta_l)$ consists of a single horizontal scale l. The velocity field of this scale is calculated from ζ_l^f using the diagnostic relations between the streamfunction and vorticity, and the velocities and the streamfunction. The inversion of the high-order elliptic equations in (5) is accomplished by splitting the high-order Laplacians into multiple Laplacian operators with the complex coefficient (Cheong et al. 2004).

Figure 7 shows the distribution of Kinetic Energy (KE) per unit mass with the horizontal scale for different resolutions at day 10. It is clear that KE curves for different resolutions exhibit similar distributions for low total-

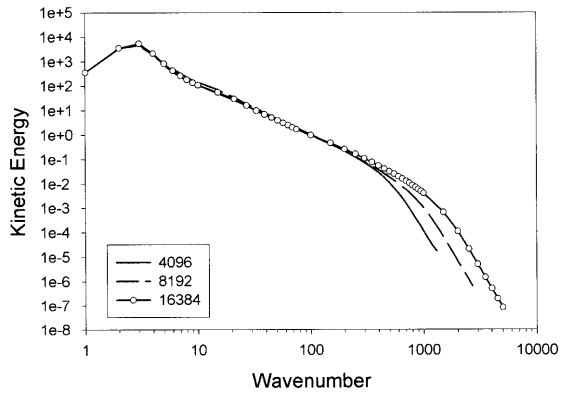

Fig. 7. Distribution of Kinetic Energy per unit mass as a function of the total wavenumber at day 10 for M1364 (4096), M2728 (8192) and M5460 (16384), respectively.

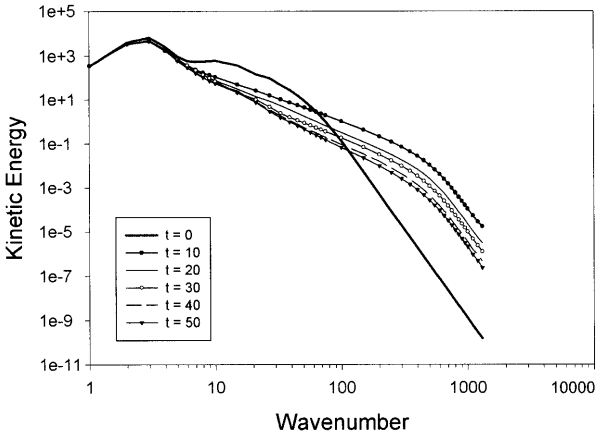

Fig. 8. Distribution of Kinetic Energy per unit mass as a function of time at selected days for the resolution of M1364 ($I = 4096$).

wavenumbers, but different distributions for high wavenumbers. As is expected, the high-resolution case shows a higher-level KE at high wavenumbers due to the low viscosity. One can easily find two distinct wavenumber subranges, each having a constant slope: One is the subrange $10 < l < L_s$, where L_s is about 300 for $I = 4096$ but increases as the resolution (for convenience, referred to as subrange I). In this subrange KE curve is slightly steeper than the l^{-2} curve, being estimated as $l^{-7/3}$ (cf. Yoden and Yamada 1993). The other is the subrange near the largest wavenumber (truncation limit) of the models, where the slope falls between l^{-6} and l^{-7} (for convenience, referred to as subrange V).

Figure 8 presents the distribution of KE per unit mass with the horizontal scale at various time stages for $I = 4096$. Except the initial stage, all curves exhibit very similar distributions one another, but with decreasing KE level at later time stages, due to viscosity. Initial KE in the wavenumber interval around $5 < l < 70$ is redistributed to the high wavenumber domain. However, KE at $l \leq 5$ is almost unchanged with time, except that KE has decreased quite a little. Although KE decreases with time, the slope of the subrange V remains almost unaltered. The slope in subrange I, however, increases slightly with time and the slope at day 50 is very close to l^{-3}, around $20 \leq l \leq 300$.

It would be worthy to compare the results to those of Yoden and Yamada (1993), where decaying two-dimensional turbulence was investigated numerically. They adopted a viscosity of biharmonic operator. The slope for subrange I in Yoden and Yamada (1993) is larger than that of this study, whereas the slope for subrange V is smaller than this study. Of course, the whole wavenumber range in Yoden and Yamada corresponds to the subrange I in this study, because the resolution in this study is higher by one or two orders. If we adopted a lower resolution model than those shown in Figs. 7 and 8, it is certain that the high-wavenumber part of subrange I in Figs. 7 and 8 is divided into two subranges. Unlike the result of Yoden and Yamada (1993), the shift of spectral peak toward low wavenumber was not found in our cases. The spectral peak associated with the zonal shears (the first peak of initial stage in Fig. 8) does not change significantly with time, while the second peak associated with the initial perturbations disappears during time evolution.

As stated above, the slope approaches l^{-3} in the later stage, but the wavenumber range in this study is much broader, and shifted toward smaller scales compared to that of Yoden and Yamada (1993), probably because of difference in model resolution and resolution-dependent viscosity. Note that the final stage of Yoden and Yamada (1993) is characterized by multiple large-scale vortices, while in the present study it is characterized by a single large vortex in each hemisphere.

6. Conclusions

We have applied a very high-resolution DFS spectral model to the two dimensional shear instability on the sphere, where the equivalent grid size is approximately 3.75 km $\times$ 3.75 km (16384 $\times$ 8192 transform grids) for the highest resolution. It was demonstrated that the DFS model performs with high accuracy (well conserving KE) and efficiency even for the large problem size without any numerical instability. Since the solution of vorticity equation, though being simple, requires important algorithms such as inversion and nonlinear terms evaluation, the results suggest that the DFS spectral method could be extended to the 3 dimensional problem with ease.

Global absolute-vorticity fields associated with the shear instability of double shear flow, were found to be similar to one another for the three resolutions (M1364, M2728 and M5460) because the large scale pattern is dominant. However, it was possible to find clear differences among the vorticity field simulated with different resolutions. As the resolution increases, more elongated (or thinner) vortex filaments were observable along with the small-scale isolated vortices. For low resolutions, thin vortex filaments are easily diffused away, due to relatively large dissipation rate compared to the high resolution simulation.

A test for the numerical convergence of the solution in terms of the time-averaged zonal-mean flow indicated a good convergence property, in spite of flow pattern itself fluctuates with a large amplitude.

The kinetic energy per unit mass showed two distinct subranges, each with a constant slope. For the subrange V (near the short wave limits; viscous subrange) the slope does not change significantly with time. On the other hand, the slope for subrange I (longer wave range beyond the subrange V) becomes steeper with time, and it approaches l^{-3} for the total wavenumbers between 20 and 300 in the later stage, when a single large vortex is formed. As the resolution increases, the subrange other than the viscous subrange extends to the higher wavenumber domain, due to low viscosity. The high resolution model used in this study made it feasible to get a KE distribution under a single dynamical system over a broad wavenumber range, even from 1 to about 5000 in total wavenumber on the sphere.

Through a series of numerical simulations on NEC SX-5, parallel vector processors having maximum vector length of 512, it was shown that the DFS model is reasonably scalable over the wide range of problem size, and also satisfactory in the aspect of parallel speedup: The CPU time closely follows theoretically expected value and the execution rate increases slightly with the resolution. The execution rate is 4.8 GFLOPS in average, being 48% of the peak performance, when one CPU is used. The parallel speedup increases with the resolution and reaches the maximum value of 5.55 at 7 CPUs for the highest resolution, but the scaled speedup decreases with the number of CPU.

When the problem becomes more complicated, the parallel performance obtained in this study may be changed. However, since the major algorithms constituting the DFS model, the inversion and double Fourier transform, can be programmed with two dimension array, in practice the easiness and efficiency of parallel implementation will be still reserved along with the efficiency in the serial computing.

Acknowledgment

The authors would like to acknowledge the support from the KISTI (Korea Institute of Science and Technology Information) under "the 3rd Strategic Supercomputing Applications Support Program". Dr. Ji-Hoon Jang at Supercomputing Center of KISTI is appreciated for the technical support for parallel computing. A part of test-runs of the numerical model were performed on the NEC SX-5 in the Korea Meteorological Administration (KMA). Anonymous reviewers are acknowledged for their useful comments.

Appendix

Inversion of the $N/2 \times N/2$ tridiagonal matrix A in the linear equations $A\boldsymbol{x} = \boldsymbol{B}$ is considered, where $\boldsymbol{x}$ and $\boldsymbol{B}$ are column vectors of $N/2$ elements. Although the algorithm for the band-diagonal matrices inversion is well known (e.g., Press et al. 1996), a detailed program is illustrated with an emphasis on the loop-ordering, because the problem considered in this study formally deals with the four dimension data. The matrices for all zonal wavenumbers are stored in a single array $A(M/2, 3, N/2, 4)$ to facilitate the vectorization. (The wave components are divided into four categories as the last array axes depending on whether the zonal and meridional wave indices are even or odd.) Be sure that for all m, $A(m, i, n, j) = 0$ with $(i, n) = (3, 1)$ and $(3, N/2)$. Then, the vectorized routine to modify A into the upper 2-band diagonal matrices is given as following. In this code, the loop-ordering for the second and third index was determined with care to maximize the efficiency of the computations (see Sabot 1995).

```
DO j=1,4
do n0=1,N/2-1
     n1=n0+1
  do m=1,M/2
            ram=A(m,1,n1,j)/
                A(m,1,n0,j)
    A(m,1,n0,j)=A(m,1,n0,j)*ram
    A(m,2,n0,j)=A(m,2,n0,j)*ram
    A(m,2,n1,j)=A(m,2,n1,j)-
                A(m,2,n0,j)
    A(m,1,n1,j)=A(m,2,n1,j)
    A(m,2,n1,j)=A(m,3,n1,j)
    A(m,3,n0,j)=ram
  end do
end do
END DO
```

Note that the second array axes is not loop-nested to maintain the vector execution for the first array axes. This should be also the case for the pentadiagonal matrices inversion where the array size of the matrix is $A(M/2, 5, N/2, 4)$. The vector $\boldsymbol{B}$ has to be modified before the backward substitution to solve for $\boldsymbol{x}$ using the elements stored in the array A.

```
DO j=1,4
do n0=1,N/2-1
     n1=n0+1
  do m=1,M/2
     B(m,n0,j)=B(m,n0,j)*A(m,3,n0,j)
     B(m,n1,j)=B(m,n1,j)-B(m,n0,j)
  end do
end do
END DO
```

References

Chandra, R., L. Dagum, D. Kohr, J. McDonald, D. Maydan, and R. Menon, 2000: *Parallel programming in OpenMP*. Morgan Kaufmann Publishers, 300pp.

Cheong, H.-B., 2000a: Double Fourier series on a sphere: Applications to elliptic and vorticity equations. *J. Comput. Phys.*, **157**, 327–349.

———, 2000b: Application of double Fourier series to shallow water equations on a sphere. *J. Comput. Phys.*, **165**, 261–287.

———, In-Hyuk Kwon, Tae-Young Goo, and Myeong-Joo Lee, 2002: High-order spectral filter with the double Fourier series on a sphere. *J. Comput. Phys.*, **177**, 313–335.

———, In-Hyuk Kwon, and Tae-Young Goo, 2004: Further study on the high-order double-Fourier-series spectral filtering on a sphere. *J. Comput. Phys.*, **193**, 180–197.

Cortese, T.A. and S. Balachandar, 1995: High performance spectral simulation of turbulent

flows in massively parallel machines with distributed memory. *Internat. J. Supercomput. Appl.*, **9**, 187–204.

Gates, W.L. and coauthors, 1992: The atmospheric model intercomparison project. *Bull. Amer. Meteor. Soc.*, **73**, 1962–1970.

Gropp, W., E. Lusk, and A. Skjellum, 1997: *Using MPI: Portable parallel programming with the message-passing interface*. The MIT Press, 307pp.

Held, I.M. and M.J. Suarez, 1994: A proposal for the intercomparison of the dynamic cores of atmospheric general circulation models. *Bull. Amer. Meteor. Soc.*, **75**, 1825–1830.

Hortal, M. and A.J. Simmons, 1991: Use of reduced Gaussian grids in spectral models. *Mon. Wea. Rev.*, **119**, 1057–1074.

Ilin, A. and L.R. Scott, 1996: Loop splitting for high performance computers. *Internat. J. Supercomput. Appl.*, **10**, 336–340.

Jakob, R., J. Hack, and D.L. Williamson, 1995: Spectral transform solutions to the shallow water test set. *J. Comput. Phys.*, **119**, 164–187.

Orszag, S.A., 1970: Transform method for the calculation of vector-coupled sums: Application to the spectral form of the vorticity equation. *J. Atmos. Sci.*, **27**, 890–895.

Press, W.H., S.A. Teukolsky, W.T. Vettering, and B.P. Flannery, 1996: *Numerical Recipes in FORTRAN 90*, Cambridge University Press, 1486pp.

Ronchi, C., R. Iacono, and P.S. Paolucci, 1996: The "cubed sphere": A new method for the solution of partial differential equations in spherical geometry. *J. Comput. Phys.*, **124**, 93–114.

Sabot, G.W., 1995: *High performance computing: Problem solving with parallel and vector architectures*. Addison-Wesley Publishing Company, 246pp.

Spotz, W.F., M.A. Taylor, and P.N. Swartztrauber, 1998: Fast shallow water equation solvers in latitude-longitude coordinates. *J. Comput. Phys.*, **145**, 432–444.

Stuhne, G.R. and W.R. Peltier, 1996: Vortex erosion and amalgamation in a new model of large scale flow on the sphere. *J. Comput. Phys.*, **128**, 58–81.

Taylor, M.A., J. Tribbia, and M. Iskandarani, 1997: The spectral element method for the shallow water equations on the sphere. *J. Comput. Phys.*, **130**, 92–108.

Yoden, S. and M. Yamada, 1993: A numerical experiment on two-dimensional decaying turbulence on a rotating sphere. *J. Atmos. Sci.*, **50**, 631–643.